Fragile topological phase on the triangular kagome lattice and its bulk-boundary correspondence

Yun-Feng Chen (陈云峰)[1] and Dao-Xin Yao (姚道新)[1,2,*]

[1]*State Key Laboratory of Optoelectronic Materials and Technologies, Guangdong Provincial Key Laboratory of Magnetoelectric Physics and Devices, School of Physics, Sun Yat-Sen University, Guangzhou 510275, China*
[2]*International Quantum Academy, Shenzhen 518048, China*

We predict and examine various topological states on a two-dimensional triangular kagome lattice (TKL) using the tight-binding models and theory of topological quantum chemistry (TQC). First, on the basis of TQC, we diagnose band structures with fragile topology and calculate Wilson-loop spectra and Hofstadter butterfly spectra to confirm their nontrivial nature. Second, we examine the bulk-boundary correspondence and find that an obstructed atomic limit (OAL) insulator hosts fractional corner states without being accompanied by fragile topological band structures, which implies that the presence of OALs and corner states is not a sufficient condition to fragile topology. Last but not least, we predict a topological phase transition from a second-order topological phase to a first-order topological phase that can be realized in the TKL under the action of a magnetic field.

I. INTRODUCTION

Since the discovery of integer quantum Hall effect, robust bulk-boundary correspondence has become a hallmark of nontrivial topology. Later, the discovery of high-order topological insulators enriched the physics with robust high-order bulk-boundary correspondence (e.g., bulk-hinge correspondence and bulk-corner correspondence) [1–8], namely, an (N-n)-order topological insulator is an N-dimensional insulator which hosts topological states on its n-dimensional boundaries.

Recently, however, this seemingly complete scheme has been challenged by the fact that fragile topological phases (FTPs) violate the bulk-boundary correspondence and only host chiral edge states under some specific twisted boundary conditions [9–32]. In addition, those widely used topological invariants that have been proposed to diagnose stable nontrivial topology (e.g., Chern number and Kane-Mele invariant) fail to capture the FTPs because of the fragility of these phases manifested by the addition of trivial bands [16–21]. More specifically, the Wannier obstructions of the FTPs (i.e., the topological obstacles that prevent FTPs from transforming into atomic limits which are described by exponentially localized Wannier functions) can be resolved only by coupling these phases with trivial bands, which is totally outside the K-theory framework.

In this situation, the theory of topological quantum chemistry (TQC) has been developed to characterize the fragile topology of FTPs [16–21]. Its central idea is to construct mappings from real-space orbitals to momentum-space topology. According to this theory, a set of exponentially localized, decoupled orbitals on maximal Wyckoff positions (the high-

symmetry positions of a space group) in the real space can induce a nonlocal space-group representation in the momentum space, which is the so-called band representation (BR) or elementary band representation (EBR) [16–21]. Mathematically, a BR is a direct sum of EBRs. A band structure shares the first-order triviality of an atomic limit if its irreducible representations of the point groups at the momenta in the first Brillouin zone (BZ) are the same as those of a BR; otherwise, this band structure carries nontrivial topology [16].

The irreducible representations of the point groups at the momenta in the first BZ determine whether a band structure shares the first-order triviality of an atomic limit or carries nontrivial (first-order or fragile) topology [16]. If a band structure's irreducible representations match those of a band representation, its first-order topology is trivial. Otherwise, it is topologically nontrivial.

To be more precise, a subtraction of EBRs, which topologically cannot be transformed into a BR, maps to a set of fragile topological bands (FTBs), and a representation outside the first-order trivial and fragile-topological classes maps to a band structure with stable first-order topology [16]. The former mapping properly manifests the fragility of fragile topology: the obstruction of transforming a subtraction of EBRs into a BR disappears after the addition of those EBRs that have been subtracted.

The subtraction of EBRs represents a split band structure that consists of two subspaces: in most cases, the lower one is fragile topological and the upper one possesses a "practical" Wannier obstruction [33–37], namely, electronic bands with this obstruction adiabatically connect to the so-called obstructed atomic limits (OALs) [16] where the localized orbitals do not coincide with any of the ionic sites in the unit cell. These bands are hereafter referred to as OALs for simplicity.

According to Refs. [6–8], an OAL directly brings about a second-order topology because of the special position of
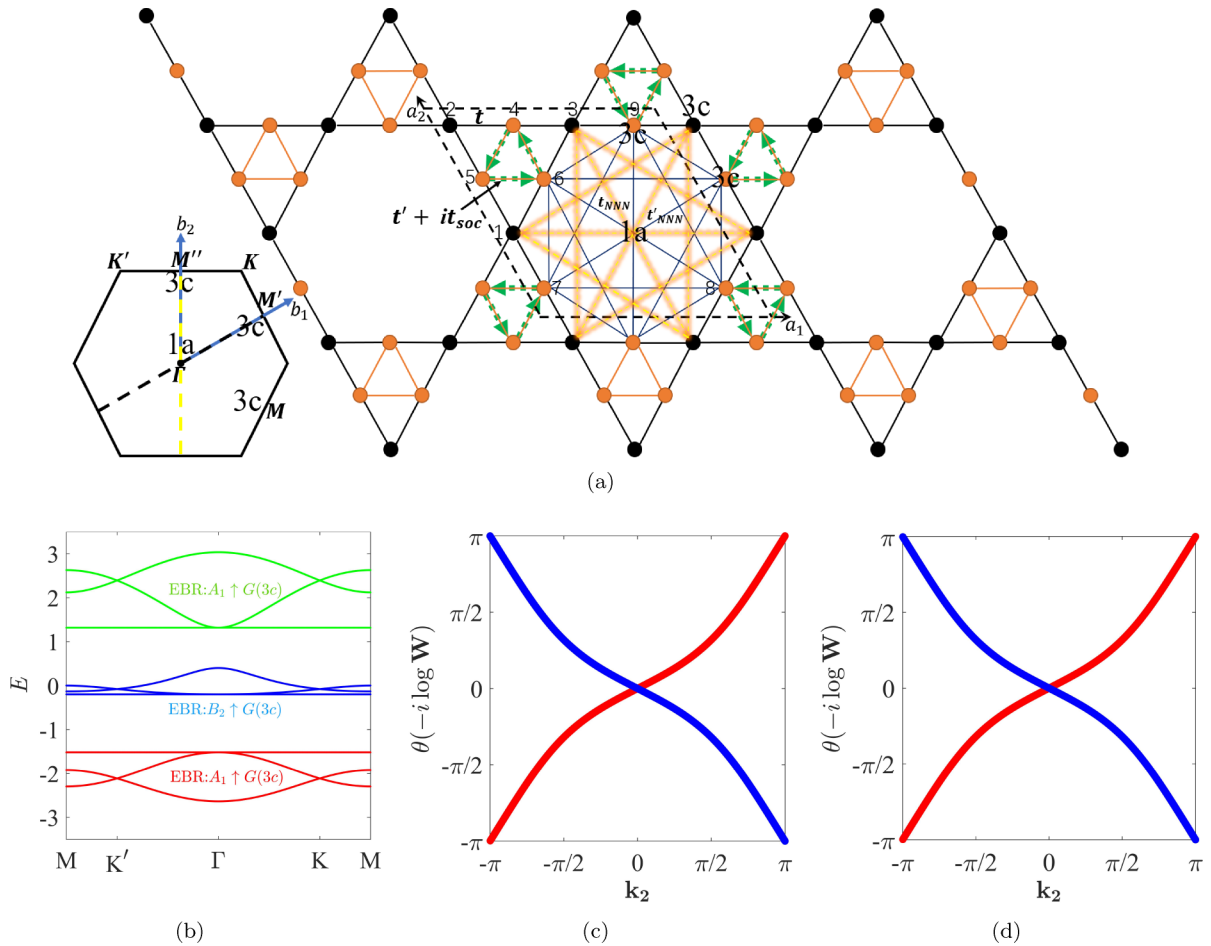
*yaodaox@mail.sysu.edu.cn

FIG. 1. (a) Diagram of a TKL and its first BZ. a_1, a_2, b_1, b_2 are basis vectors in real space and momentum space, respectively. NN hoppings with energies t and t' are represented by black and orange bonds, respectively. NNN hoppings with energies t_{NNN} and t'_{NNN} are represented by yellow dashed and blue solid bonds, respectively. Those anticlockwise Haldane-model-like hoppings with energy t_{SOC} are represented by green dashed arrows. Wyckoff positions $1a$ and $3c$ are indicated in this diagram. (b) Band structure of H_{NN}^{TB} along the path $M - K' - \Gamma - K - M$ (in $b_1 + b_2$ direction), with $t = 1$ and $t' = 0.2t$. The top, middle, and bottom groups and their corresponding EBRs are indicated in this spectrum. [(c), (d)] Wilson-loop spectra of the upper and lower sets of FTBs. Red and blue spectral lines belong to different FTBs from the same set. Despite that the upper set is flatter than the lower set, they exhibit the same Wilson-loop spectrum because of their identical momentum-space representations. The Wilson loop along b_2 and the integral loop along b_1 are indicated by yellow and black dashed lines in BZ, respectively.

its Wannier center, which also gives rise to extra fractional charge distribution on the corners of a finite lattice (details are demonstrated in Appendix A). Therefore, when a FTP is complementary to an OAL (i.e., all the bands under the OAL, including the FTBs, are filled), it hosts fractional corner states under open boundary conditions [33–37].

As for higher-order topology, it is actually included in the first-order trivial class because the OALs can exhibit nontrivial higher-order topology that can be identified through TQC methods. The term "stable topology" is commonly used to refer to first-order topology, and there is no reasonable definition of whether a second-order topological phase (SOTP) is stable or not. For example, we can consider coupling a two-dimensional SOTP with a two-dimensional first-order topological phase (with a Chern number of 1), and the original zero-dimensional corner states will be replaced by one-dimensional edge states. The SOTPs of the first-order topological phase (FOTP) are trivial, but coupling it with a SOTP makes the second-order phase disappear. According to the definition of fragile topology, it seems that this SOTP

should be defined as a second-order fragile topological phase. However, when this process also can be seen as coupling an OAL with a Chern band, it ultimately results in a multiband structure with a Chern number of 1 and cannot be determined as a certain fragile topology using TQC methods. Therefore, because of the lack of clear definition, in this paper stable topology is only used to refer to first-order topology.

Although stable topological invariants fail to distinguish FTPs from normal trivial phases, there are clear differences between them. For example, FTPs react differently towards a perpendicular magnetic field. In this magnetic field, electrons on 2D lattices exhibit a kind of fractal structure in energy spectra called the Hofstadter butterfly [38]. Since the Landau levels (LLs) of a set of trivial electronic bands are bounded inside the energy span of this set in the zero-field limit, the Hofstadter butterfly of a trivial set shall never connect to the one of another trivial set if these sets are isolated from each other before the presence of the magnetic field. Interestingly, FTPs exhibit connected Hofstadter butterfly spectra, which manifests their nontrivial nature [12–15,37,39–41].

TABLE I. The irreducible representations at Γ, K, and M for the three groups of bands, the two sets of FTBs, and the three EBRs of $P6mm$. By comparing these irreducible representations, we find that the top and bottom groups match the EBR $A_1 \uparrow G(3c)$ and the middle one matches $B_2 \uparrow G(3c)$. Similarly, we subtract $A_1 \uparrow G(1a)$ from $A_1 \uparrow G(3c)$ and obtain the representations of the two sets of FTBs. The notations used here are from the Bilbao Crystallographic Server [51–53]. The number in brackets behind an irreducible representation denotes its dimensions, and the letter in brackets behind an EBR denotes the Wyckoff positions wherefrom this EBR is induced.

Trivial bands	Γ	K	M
Top group	$\Gamma_1(1) \oplus \Gamma_5(2)$	$K_1(1) \oplus K_3(2)$	$M_1(1) \oplus M_3(1) \oplus M_4(1)$
Middle group	$\Gamma_4(1) \oplus \Gamma_6(2)$	$K_2(1) \oplus K_3(2)$	$M_1(1) \oplus M_2(1) \oplus M_4(1)$
Bottom group	$\Gamma_1(1) \oplus \Gamma_5(2)$	$K_1(1) \oplus K_3(2)$	$M_1(1) \oplus M_3(1) \oplus M_4(1)$
EBRs			
$A_1 \uparrow G(3c)$	$\Gamma_1(1) \oplus \Gamma_5(2)$	$K_1(1) \oplus K_3(2)$	$M_1 \uparrow M_3(1) \oplus M_4(1)$
$B_2 \uparrow G(3c)$	$\Gamma_4(1) \oplus \Gamma_6(2)$	$K_2(1) \oplus K_3(2)$	$M_1(1) \oplus M_2(1) \oplus M_4(1)$
$A_1 \uparrow G(1a)$	$\Gamma_1(1)$	$K_1(1)$	$M_1(1)$
FTBs			
Upper set	$\Gamma_5(2)$	$K_3(2)$	$M_3(1) \oplus M_4(1)$
Lower set	$\Gamma_5(2)$	$K_3(2)$	$M_3(1) \oplus M_4(1)$

Moreover, FTPs also exhibit nontrivial windings of Berry phases in Wilson-loop spectra, which definitely indicates their nontrivial topology. Therefore, these spectra have been widely analyzed to study the difference between FTPs and normal trivial phases. In this paper, we focus on examining the FTP on a triangular kagome lattice (TKL) [42–50] and its bulk boundary correspondence. Compared to the kagome lattice, we find that the more frustrated structure of the TKL becomes an advantage for hosting various topological states since more complicated Wannier obstructions can be created. Last but not least, we also find a topological phase transition from a SOTP to a FOTP that can be realized in this lattice.

The rest of this paper is organized as follows: In Sec. II A, we use the theory of TQC to diagnose the band topology of several tight-binding (TB) models on a TKL. We compute the Wilson-loop spectra of two sets of FTBs in Sec. II B and examine the bulk-boundary correspondence in Sec. II C. In Sec. III A, we compute the Hofstadter butterfly spectra and discuss their bounded and connected patterns. In Sec. III B, we demonstrate how to realize the transition from a SOTP to a FOTP by increasing the magnetic field strength. Finally, we conclude in Sec. IV.

II. FRAGILE TOPOLOGICAL BANDS AND BULK-BOUNDARY CORRESPONDENCE

A. Symmetry analysis based on TQC

First, we consider a spinless nearest-neighbor (NN) TB model on the TKL [see Fig. 1(a)],

$$H_{\text{NN}}^{\text{TB}} = \sum_{<i,j>} \left[t \sum_{\alpha,\beta} C_{i,\alpha}^\dagger C_{j,\beta} + t' \sum_{\beta',\beta} C_{i,\beta'}^\dagger C_{j,\beta} \right] + \text{H.c.}, \quad (1)$$

where $\langle \rangle$ denotes that only the hoppings between nearest sites are considered in this summation. The lattice sites of the small and big triangles in the unit cell are labeled by $\alpha(\alpha')$=1, 2, 3 and $\beta(\beta')$=4, 5, 6, 7, 8, 9, respectively. To be specific, in Fig. 1(a), black dots labeled by 1, 2, 3 form the big triangles, and orange dots labeled by 4, 5, 6 or 7, 8, 9 form the small triangles. The space group of the TKL is $P6mm$ (No. 183), and

the point groups of the three high-symmetry momenta in the BZ [i.e., Γ=(0,0), K = $(\frac{2\pi}{3}, \frac{2\pi}{3})$, M = $(\frac{\pi}{2}, 0)$] are C_{6v}, C_{3v}, and C_{2v}, respectively.

To be representative, we assume that the energies of the hoppings along the black and orange bonds in Fig. 1(a) is are $t = 1$ and $t' = 0.2t$, respectively. The resulting band structure is shown in Fig. 1(b), where the nine bands are divided into the top, middle, and bottom groups. By calculating the irreducible representations (see Table I), we determine that the top and bottom groups are represented by the EBR $A_1 \uparrow G(3c)$ and the middle group is represented by $B_2 \uparrow G(3c)$. These two EBRs are induced by orbitals localized on the $3c$ Wyckoff positions [see Fig. 1(a)] in the unit cell, where ionic sites coincide with the centers of the orbitals. Therefore, no OAL is created and these groups of bands are normally trivial. Next, We introduce the next-nearest-neighbor (NNN) hoppings shown in Fig. 1(a) into the TB model to create FTB structures:

$$H_{\text{NNN}}^{\text{TB}} = H_{\text{NN}} + H_{\text{NNN}}, H_{\text{NNN}}$$

$$= \sum_{\langle\langle i,j \rangle\rangle} \left[t_{\text{NNN}} \sum_{\alpha,\alpha'} C_{i,\alpha}^\dagger C_{j,\alpha'} + t'_{\text{NNN}} \sum_{\beta',\beta} C_{i,\beta'}^\dagger C_{j,\beta} \right] + \text{H.c.}, \quad (2)$$

where $\langle\langle \ \rangle\rangle$ denotes that the hoppings between next-nearest sites are also considered in this summation. In this paper, the term next-nearest hopping refers specifically to the hopping between two $\alpha(\beta)$ sites, not the hopping between one α and one β site. The latter is useless for creating FTBs and therefore ignored. With the parameters of the NN hoppings unchanged, we set the parameters of the NNN hoppings between α sites and between β sites to be $t_{\text{NNN}} = 0.6t$ and $t'_{\text{NNN}} = 0.4t'$, respectively.

The resulting band structure is shown in Fig. 2(a), where the top and bottom groups are both split into an OAL and a set of FTBs (i.e., a two-band subspace hosting fragile topology), and the middle group remain unchanged, still represented by $B_2 \uparrow G(3c)$. The two sets of FTBs, called the upper and lower sets, are represented by the same subtraction of EBRs (see Table I): $A_1 \uparrow G(3c) \ominus A_1 \uparrow G(1a)$. It indicates that they
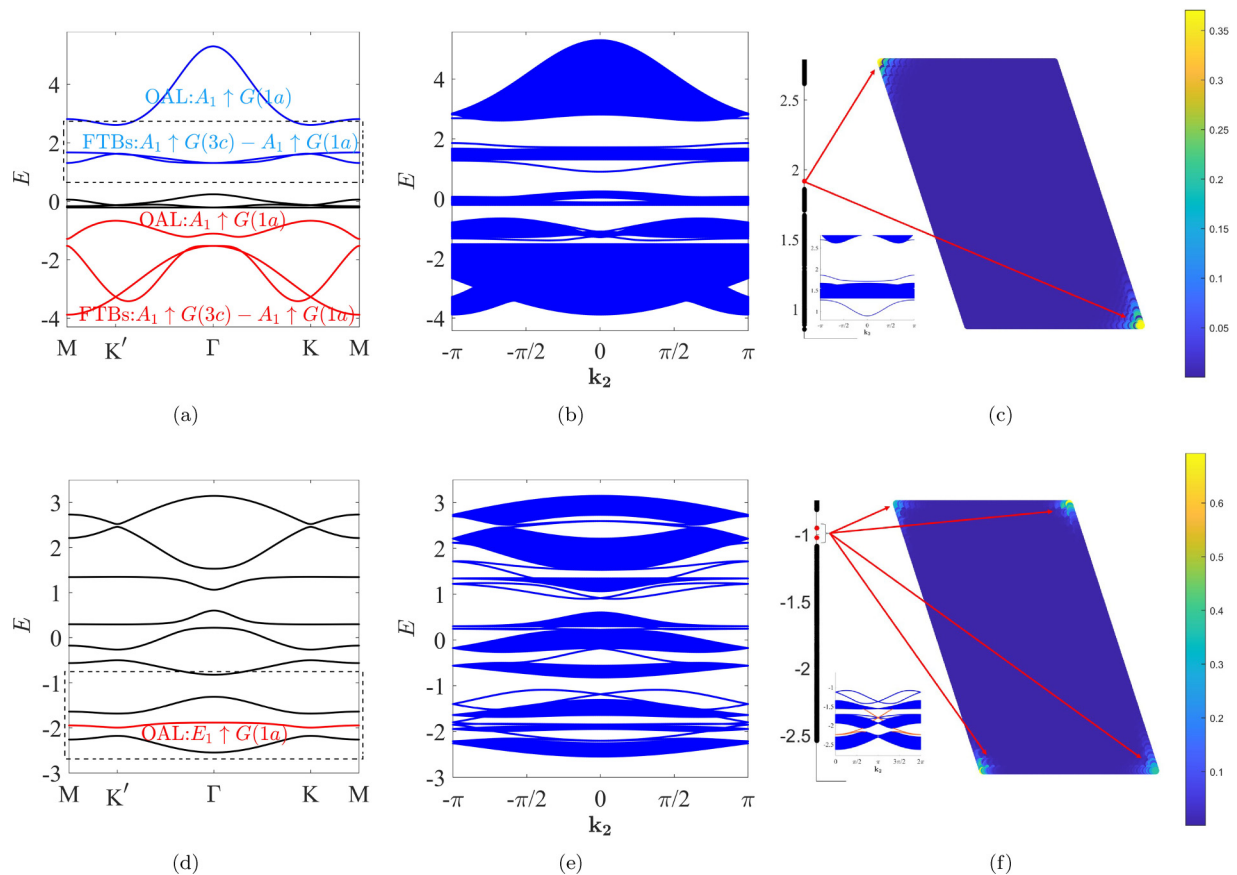
FIG. 2. (a)–(c) Band structures of $H_{\mathrm{NNN}}^{\mathrm{TB}}$ for (a) periodic boundary conditions, (b) open boundary condition in $\boldsymbol{a_1}$ direction ($L_1 = 200$), and (c) open boundary conditions in $\boldsymbol{a_1}$ and $\boldsymbol{a_2}$ directions ($L_1 = L_2 = 30$), with $t_{\mathrm{NNN}} = 0.6t$, $t'_{\mathrm{NNN}} = 0.4t'$, and $t'=0.2t$. (d)–(f) Similar band structures of $H_{\mathrm{SOC}}^{\mathrm{TB}}$ with $t_{\mathrm{SOC}} = 0.3t$ and $t'=0.3t$. In (c) and (f), the energy spectrum on the left shows the fractional corner states marked by red dots, and the diagram on the right shows the distribution of the corner states on the 30×30 TKL. Chiral edge states appear in (e), and those in the first and second gaps (counted from the bottom) are redrawn and highlighted in red in the inset in (f). Black dashed rectangles in (a) and (d) draw the energy ranges of the spectra and insets in (c) and (f), respectively.

are indeed fragile topological, which can be confirmed by calculating the Wilson-loop spectrum (see Sec. II B). As for the band represented by $A_1 \uparrow G(1a)$, it is identified as an OAL since no ionic site coincides with the $1a$ Wyckoff position in the unit cell [see Fig. 1(a)]. Even though the band structure seems to be completely changed, all the degeneracies at high-symmetry points are still preserved because the space-group symmetry remains unchanged. Besides, the NNN hoppings have no effect on time-reversal symmetry $\mathcal{T}$ because of their real hopping parameters.

B. Wlison loop spectra

Even though the two sets of FTBs both have a zero Chern number, their nontrivial topology can be manifested in the Wilson-loop spectrum. First, we define the Wilson-loop operator $w_{\boldsymbol{k}}$ [23], which is constructed by the wave functions ψ^1 and ψ^2 of the two FTBs from the same set,

$$w_{\boldsymbol{k}} = \left[\psi^1_{\boldsymbol{k}}, \psi^2_{\boldsymbol{k}} \right], \tag{3}$$

where $\boldsymbol{k} = k_1 \boldsymbol{b_1} + k_2 \boldsymbol{b_2}$, with $k_1, k_2 \in [0,2\pi]$. This operator is discretized into N^2 operators when periodic conditions are

applied to the boundaries of a N × N TKL. Next, while keeping k_2 fixed, we multiply all the discretized Wilson operators along an integral loop in the $\boldsymbol{b_1}$ direction [23]:

$$W(k_2) = \prod_{n=0}^{N-1} w^{\dagger}_{\frac{n \cdot 2\pi}{N}, k_2} \times w_{\frac{(n+1) \cdot 2\pi}{N}, k_2}. \tag{4}$$

By calculating the eigenvalues of $-i \ln W(k_2)$, we obtain the Berry phases of the two FTBs along the one-dimensional integral loop that starts at $(0, k_2)$. As k_2 circulates around the Wilson loop (i.e., a closed path around the BZ along $\boldsymbol{b_2}$ direction), the one-dimensional Berry phases of the two FTBs evolve from $-\pi$ (π) to π ($-\pi$) as shown in Figs. 1(c) and 1(d), contributing opposite winding numbers (n = ±1). This is a $\mathbb{Z}$ classification introduced in the Wilson loop to diagnose the topology of connected subspaces in which every band crosses with each other.

In fact, it is the combined symmetry $C_{2z}\mathcal{T}$ that protects these nontrivial windings [17,21,23]. Here are the reasons: (1) After the addition of the NNN hoppings, $\mathcal{T}$ is still preserved and enforces the Chern number of each set of FTBs to be zero, which consequently protects the opposite winding numbers.

TABLE II. C_{2z} eigenvalues of the two sets of FTBs at Γ and M.

FTBs	Γ	M
Upper set	2	-2
Lower set	2	-2

(2) By calculating the C_{2z} eigenvalues of each set of FTBs in the BZ, we find that the signs of these eigenvalues are opposite at Γ and M (see Table II). This difference of a minus sign symbolizes a phase difference of π between the wave functions at the two points, which explains the nontrivial windings of Berry phases from Γ to M along the Wilson loop. (3) In this 2D spinless model, C_{2z} rotates $\boldsymbol{k}$ to $-\boldsymbol{k}$ around the out-of-plane $\mathbf{z}$ axis and $\mathcal{T}$ reverses $-\boldsymbol{k}$ back to $\boldsymbol{k}$, keeping every momentum $\boldsymbol{k}$ in the BZ fixed. Therefore, $C_{2z}\mathcal{T}$ is preserved everywhere in the BZ, including in the Wilson loop. As a result, the continuity of the evolution of the Berry phases along this loop is ensured by this combined symmetry.

C. Fractional corner states hosted by an OAL insulator

We apply the open boundary conditions in $\boldsymbol{a_1}$ and $\boldsymbol{a_2}$ directions to cut the TKL into a 30×30 lattice and then calculate the energy spectrum of $H_{\text{NNN}}^{\text{TB}}$ to examine the bulk-boundary correspondence of the FTBs. The results are shown in Fig. 2(c), where two isolated degenerate states appear in the gap above the upper set of FTBs. By looking into the distribution of their wave functions on the finite TKL, we determine that these states are SOTPs with fractional distribution at the corners, which, according to Refs. [6–8,33–37], are created by the OAL above them. (see more details in Appendix A).

Given that FTBs are always accompanied by OALs, one might expect this second-order bulk-corner correspondence to be a fingerprint of FTPs. However, we find that an OAL and its corner states appear without the accompany of FTBs, which implies that the presence of OALs is not a sufficient condition to the fragile topology. To demonstrate this phenomenon, first, we replace the NNN hoppings with the Haldane-model-like ones [see Fig. 1(a)] to break $\mathcal{T}$. These terms are still referred to as the spin-orbit-coupling (SOC) terms even though our model is spinless. They can be considered as the hoppings between orbitals with the same spin (e.g., $\uparrow$ or $\downarrow$). The TB Hamiltonian then becomes

$$H_{\text{SOC}}^{\text{TB}} = H_{\text{NN}} + H_{\text{SOC}}, H_{\text{SOC}}$$
$$= \sum_{\beta',\beta} \exp(i\phi(r_{\beta'} - r_\beta)) t_{\text{SOC}} C_{\beta'}^\dagger C_\beta + \text{H.c.}, \quad (5)$$

where $\exp(i\phi(\boldsymbol{r}_{\beta'} - \boldsymbol{r}_\beta)) = (\pm)i$ when the hoppings are anti-clockwise (clockwise), as indicated in Fig. 1(a). Apparently, these hoppings are endowed with in-plane chiralities by their phase factors. Hence, $\mathcal{T}$ is broken due to the imaginary phase factors, and all the mirror symmetries of $P6mm$ with mirror planes perpendicular to the plane of Fig. 1(a) are also broken, since no in-plane chirality is invariant after undergoing these reflections.

Consequently, the space-group symmetry is reduced from $P6mm$ (No. 183) to $P6$ (No. 168), which lifts all the degeneracies at Γ and K and splits the bottom group into three single

bands, as shown in Fig. 2(d). The middle band is an OAL represented by the EBR $E_1 \uparrow G(1a)$, whereas the other two bands cannot be represented by any one-dimensional EBRs or subtractions of EBRs and therefore carry opposite Chern numbers ($C = \pm 1$). Naturally, a pair of edge states with opposite chiralities appears in the gaps between the two bands and the OAL, as shown in Fig. 2(e). Besides, as shown in Fig. 2(f), two pairs of isolated states (each pair consists of two degenerate states) manifest themselves on the corners of the 30×30 TKL, with their energies lying in the gap above the three bands. If all the bands under this gap are filled, this system turns into an OAL insulator which hosts fractional corner states.

III. PRESENCE OF MAGNETIC FIELDS

A. Hofstadter butterfly spectra

To compute the Hofstadter butterfly spectrum, first we choose the Landau gauge $\boldsymbol{A}(\boldsymbol{r}) = (0, \phi\boldsymbol{r} \cdot \boldsymbol{a_1})$ to introduce a uniform magnetic field, where $\boldsymbol{A}$ is the magnetic vector potential and ϕ is the magnetic flux per unit cell. In this gauge, the $\boldsymbol{r}$ dependence of the nonzero component of $\boldsymbol{A}$ along the $\boldsymbol{a_1}$ direction breaks the translational invariance in this direction. However, at a commensurate $\phi = 2\pi\frac{p}{q}$ (i.e., the two integers p and q are coprime), the broken translational invariance is restored with the cost of making the unit cells q times larger. Correspondingly, the first BZ shrinks, with $k_1 \in [0, \frac{2\pi}{q}]$ and $k_2 \in [0, 2\pi]$.

In the magnetic field, every hopping along a Peierls path acquires an extra phase factor $\exp(i\theta(r - r'))$ via the Peierls substitution, where the argument $\theta(r - r')$ can be calculated through an integral along the Peierls path [37]:

$$\theta(r - r') = \int_{C_{r' \to r}} A(r) \cdot dr. \quad (6)$$

In this paper, we choose the Peiels paths to be straight lines connecting ionic sites. Now we give the Hofstadter Hamiltonians for the TB models on the TKL:

$$H^{\text{Hof}} = \sum_{i,j,\alpha,\beta} \exp(i\theta(r_{i,\alpha} - r_{j,\beta})) t_{i,j,\alpha,\beta} \cdot C_{i,\alpha}^\dagger C_{j,\beta} + \text{H.c.}, \quad (7)$$

where $H^{\text{Hof}} \equiv H_{\text{NN}}^{\text{Hof}} (H_{\text{NNN}}^{\text{Hof}})$ for $H_{\text{NN}}^{\text{TB}} (H_{\text{NNN}}^{\text{TB}})$. We diagonalize these Hamiltonians in the enlarged magnetic unit cell and show the resulting Hofstadter butterfly spectra in Figs. 3(a) and 3(b).

As shown in Fig. 3(b), each set of FTBs connects to its complementary OAL when the magnetic field is present, manifesting its nontrivial topology, whereas the middle group represented by the EBR $B_2 \uparrow G(3c)$ always stays bounded no matter how strong the magnetic field becomes. The black part in Fig. 3(b) indicates that the gap between the upper (lower) FTBs and OAL closes once and then opens again within the domain $(2\pi, \frac{11\pi}{4})$. Therefore, FTBs and OAL are correlated with each other and combine as an ensemble that jointly contributes to the connecting Hofstadter butterfly.

Considering that the bounded pattern of the middle group comes from its topological trivial nature, it is reasonable to expect that the top and bottom groups that are classified as $A_1 \uparrow G(3c)$ are also bounded. However, Fig. 3(a) shows the anomalous expansions of these groups, which becomes an
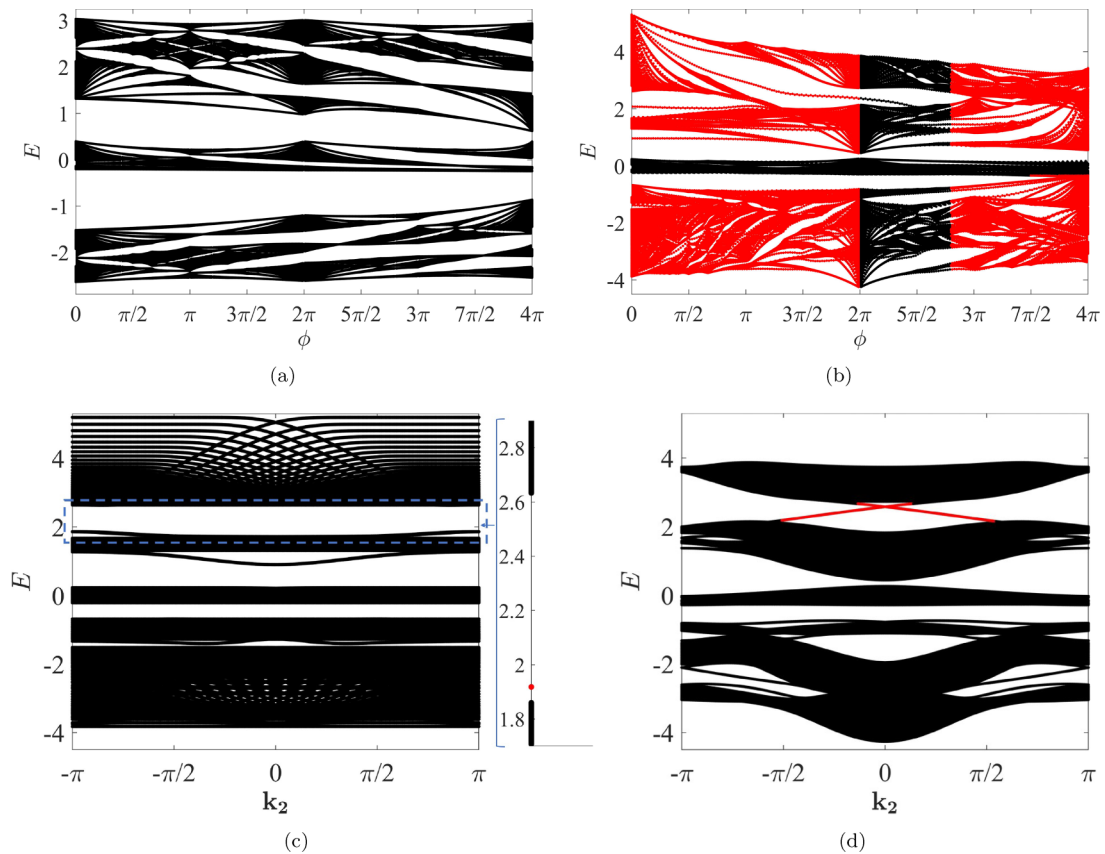
FIG. 3. (a), (b) Hofstadter butterfly spectra for (a) $H_{\mathrm{NN}}^{\mathrm{Hof}}$ and (b) $H_{\mathrm{NNN}}^{\mathrm{Hof}}$, with the same parameters of Figs. 1(b) and 2(a), respectively. In (a), the Hofstadter butterflies of the top and bottom groups expand towards the middle group. In (b), the connected parts of the Hofstadter butterflies are painted red. (c), (d) Energy spectra of $H_{\mathrm{NNN}}^{\mathrm{Hof}}$ with open boundary condition in $\boldsymbol{a}_1$ direction at (c) $\phi = \frac{2\pi}{q}$ ($q = 200$) and (d) $\phi = 2\pi$. In (c), the inset on the right exhibits two degenerate corner states marked by red dots. In (d), chiral edge states are represented by red lines.

intriguing issue. We conjecture that the $\mathcal{T}$-breaking effect of the magnetic field, which can lift the degeneracies at high-symmetry points and create isolated Chern bands [as in the case of Fig. 2(d)], causes the expansions. It also explains the connections between FTBs and OALs, since the $\mathcal{T}$-breaking magnetic field can simultaneously break $C_{2z}\mathcal{T}$ and split each set of FTBs into two Chern bands.

As for the middle group, it is immune from being affected by the magnetic field because of its solid trivial nature, i.e., this group of bands adiabatically turns into a trivial flat band when t' gradually decreases to zero. Considering that the expanded and bounded groups are represented by different EBRs, we believe that the theory of TQC may catch some implicit differences between these two trivial band structures, which are waiting for more explorations.

B. Topological phase transition from a SOTP to a FOTP

The expanded and connected patterns of Figs. 3(a) and 3(b) indicate that nontrivial LLs can be shifted under the action of a magnetic field with increasing strength, which enables a topological phase transition from a SOTP to a FOTP in the TKL. First, we search for a gap wherein corner states already exist before the presence of a magnetic field. When all the levels under this gap are filled, a SOTP appears on the lattice.

After the shifts of the LLs with nonzero Chern numbers from the unoccupied subspace to the occupied subspace across the gap, a FOTP appears and exhibits topological states on edges instead of on corners, which symbolizes the completion of the transition.

On the basis of the discussion in Sec. II C, we choose the gap between the upper set of FTBs and its complementary OAL as our candidate. While the magnetic field is barely introduced ($\phi = \frac{2\pi}{q}$), the SOTP is preserved since the corner states still exist in this gap [see Fig. 3(c)]. At $\phi = 2\pi$, the Chern number of the occupied bands becomes 1 from zero and the corner states are submerged into chiral edge states [see Fig. 3(d)], which indicate the transition to the FOTP.

Generally speaking, it is difficult but not impossible to create such a strong magnetic field that squeezes a magnetic flux quantum into one unit cell. Recently, researchers have realized some many-body phases of twisted-bilayer graphene at 2π flux in experiments [54,55], encouraging us to consider realizing this transition in a twisted-bilayer TKL.

IV. CONCLUSION AND DISCUSSION

Considering the recent popularity of kagome metals [56–58] and insulators with nontrivial topology, we believe
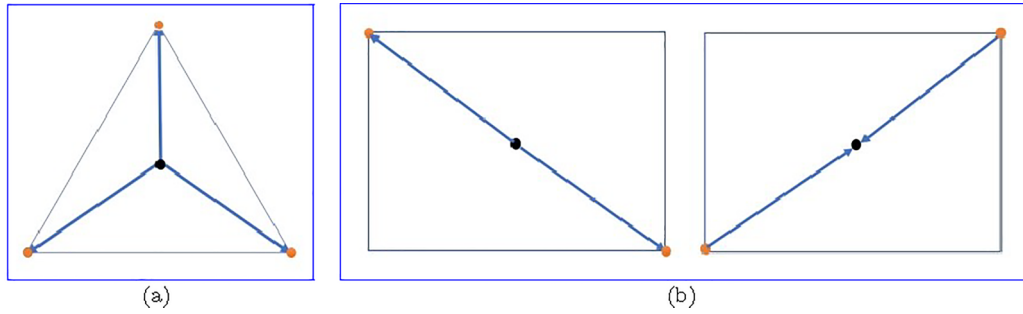
FIG. 4. FL scheme of second-order topological phases in (a) triangular lattice and (b) square lattice. Black dots represent Wannier center, orange dots represent corner states. Blue arrows are polarization vectors.

that it is of great interest to explore the topological physics behind the more frustrated kagomelike lattices, which can simultaneously enhance Wannier obstructions and the electronic correlations. Our paper is a very beginning study in this direction.

In this paper, we diagnosed the fragile topology of the two band structures with different energy spans. The windings of Berry phases and the connected Hofstadter butterflies confirm their nontrivial topology. During the calculations, we realize that magnetic fields can release implicit details of topological band structures to create and shift nontrivial LLs, which eventually gives rise to the connected Hofstadter spectrum. However, a trivial band structure represented by $A_1 \uparrow G(3c)$ also exhibits an expanded pattern in the magnetic field, which is different from the bounded group represented by $B_2 \uparrow G(3c)$. We believe that the trivial nature of the expanded group is less solid than the bounded group and that the difference between these two trivial band structures is captured by the theory of TQC, which demonstrates that a classification could exist between the trivial and fragile toplogy.

By examining the bulk-boundary correspondence, we find that the presence of OALs and corner states is not a sufficient condition of fragile topology, which makes us wonder whether it is possible to find a FTP without the presence of complementary OALs. It is of great interest to explore the bulk-boundary correspondence of this kind of FTP. Last but not least, considering that it is experimentally realizable to reach one quantum flux in the moire unit cell of twisted-bilayer structures, we are inspired to explore possible applications of the topological phase transition in a twisted-bilayer TKL.

APPENDIX A: CONNECTION BETWEEN WANNIER CENTER AND SECOND-ORDER TOPOLOGY

In this Appendix, we want to discuss the connection between the position of Wannier center and second-order topology. Benalcazar *et al.* calculated the Wilson loop of two occupied bands in a four-band model in a square lattice and found that the Berry phase of the two occupied bands did not reach $\frac{\pi}{2}$ on the entire Wilson loop [6]. This seems to imply that there is no obstructed atomic limit in the band structure of this model. However, they then used the nested Wilson loop method to reassign the two intersecting occupied bands as two separated Wannier bands and calculated the Wannier centers of these two bands, and found that both were located at (see Fig. 4) $\frac{R}{2}$, which is the middle position between two adjacent unit cells [6]. In the original paper, the polarization vectors of the Wannier bands defined by the nested Wilson loop method were calculated. This is a higher-order topological invariant, which is essentially the average of the Berry phase obtained along the $\boldsymbol{x}$ or $\boldsymbol{y}$ direction and thus equivalent to the Wannier center in physical meaning. Therefore, the Wannier centers of the occupied bands are indeed separated from the lattice sites.

Song *et al.* also discussed in detail the relationship between SOTPs in square lattices and the Wannier centers of occupied bands [7]. Ezawa further clarified this relationship by proposing a SOTP that appears in Kagome lattices [8]. Essentially, this work constructed one-dimensional SSH models on each edge of a triangular lattice and tuned them to the nontrivial phase, resulting in zero-dimensional boundary states at the corners where these SSH models intersect. The proposed second-order topological index in this paper is the sum of the squares of the polarization vectors on the three edges of the triangular lattice. Since the polarization vector is equivalent to the Wannier center, this topological index actually gives the distance between the Wannier center of the occupied band and the origin. This paper showed that in the nontrivial phase, the topological index of the occupied band (which has only one band) is $\frac{1}{2}$, indicating that the Wannier center of this band is located at (see Fig. 4) $\frac{R}{2}$. Therefore, in this second-order phase within a triangular lattice, the Wannier center of the occupied band still does not coincide with the lattice sites.

In conclusion, the separation of the Wannier center from ionic sites directly brings about second-order topology. The mechanism behind this phenomenon can be explained by the modern polarization theory which use Wannier center to de-
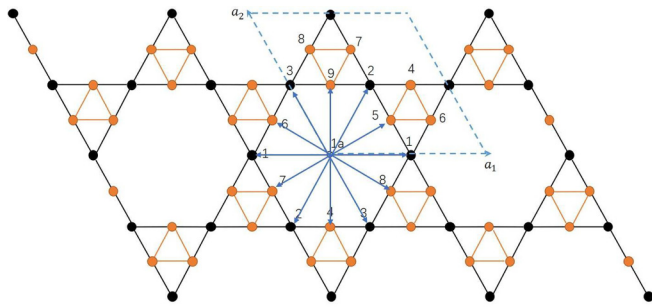
FIG. 5. Scheme of the C_{2z} rotation. Sites in different unit cells are related by the rotation: $1 \leftrightarrow 1, 2 \leftrightarrow 2, 3 \leftrightarrow 3, 4 \leftrightarrow 9, 5 \leftrightarrow 7, 6 \leftrightarrow 8$.

fine polarization vectors:

$$P = \frac{-e}{(2\pi)^3} \int_{BZ} A^{tr}(k)d^3k = \frac{-e}{V_{cell}} \sum_n^{occ} r_n \left(\mathrm{mod} \frac{eR}{V_{cell}} \right), \quad (A1)$$

where r_n is the Wannier center of the $n\{\rm\ th\}$ band in occupied subspace. The Wannier center of the occupied band located at $\frac{R}{2}$ indicates the existence of a polarization vector, pointing from the center to corners of a lattice. This results in the separation of positive and negative charges at the center and causes the charges to move along the direction of the polarization vector towards the corners, resulting in charge accumulation at the corners.

APPENDIX B: DETAILS OF THE DERIVATION FOR THE IRREDUCIBLE REPRESENTATIONS TABLE

We begin by constructing matrix representations of the symmetry operators of the $P6mm$ space group in real space. We use the same set of basis vectors as the TB Hamiltonians defined in the main text and transform these matrices into momentum space. The resulting matrices depend on wave vector k and allow us to calculate the symmetry eigenvalues of each band at every point in the BZ. By comparing the results with the character table of the point group of each k, we obtain the irreducible representations presented in Table I.

For example, under C_{2z} rotation with the $1a$ position as the center, the orbitals of the system are rotated from one site to another as shown in Fig. 5. The nonzero matrix elements of

TABLE III. Character table of the point groups of Γ and M [51–53].

Γ	E	C_{3z}	C_{2z}	C_{6z}	m_{100}	m_{120}
Γ_1	1	1	1	1	1	1
Γ_2	1	1	−1	1	−1	−1
Γ_3	1	1	−1	−1	1	−1
Γ_4	1	1	−1	−1	−1	1
Γ_5	2	−1	0	−1	0	0
Γ_6	2	−1	0	1	0	0
M	E	C_{2z}	m_{100}	m_{120}		
M_1	1	1	1	1		
M_2	1	1	−1	−1		
M_3	1	−1	−1	1		
M_4	1	−1	1	−1		

C_{2z} are contributed by sites that are related by the rotation:

$$C_{2z}(1, 1) = e^{i(k_x+k_y)}, \quad C_{2z}(2, 2) = e^{i \cdot k_y},$$
$$C_{2z}(3, 3) = e^{i(k_x+2k_y)}, \quad C_{2z}(9, 4) = e^{i(\frac{3k_x}{2}+k_y)},$$
$$C_{2z}(7, 5) = e^{i(k_x+\frac{k_y}{2})}, \quad C_{2z}(8, 6) = e^{i(\frac{3k_x}{2}+\frac{k_y}{2})}. \quad (B1)$$

Since both the point groups of Γ and M include C_{2z} symmetry, we can directly calculate C_{2z} characters of the nine bands at these two points. For an isolated band, its wave functions at these points form one-dimensional irreducible representations. Their eigenvalues are simply the characters. For the upper OAL band, its C_{2z} eigenvalues at Γ and M are both 1, and we classify its irreducible representations at Γ and M as Γ_1 and M_1, respectively, by comparing with the character table of C_{6v} and C_{2v} (Table III).

When two bands cross at Γ or M, their degenerate wave functions at these points form two-dimensional irreducible representations. We can determine the C_{2z} characters of these irreducible representations by diagonalizing their 2×2 matrix representations and summing the eigenvalues. For the upper FTB band, which has a twofold degeneracy at Γ, we find that its irreducible representation is Γ_5, since the eigenvalues are both 1 and the character is 2. By following this procedure, we can determine all the irreducible representations listed in Table I.

[1] F. Schindler, A. M. Cook, M. G. Vergniory, Z. Wang, S. S. Parkin, B. A. Bernevig, and T. Neupert, Higher-order topological insulators, Sci. Adv. **4**, eaat0346 (2018).

[2] F. Schindler, Z. Wang, M. G. Vergniory, A. M. Cook, A. Murani, S. Sengupta, A. Y. Kasumov, R. Deblock, S. Jeon, I. Drozdov *et al.*, Higher-order topology in bismuth, Nat. Phys. **14**, 918 (2018).

[3] F. K. Kunst, G. van Miert, and E. J. Bergholtz, Lattice models with exactly solvable topological hinge and corner states, Phys. Rev. B **97**, 241405(R) (2018).

[4] H. Xue, Y. Yang, G. Liu, F. Gao, Y. Chong, and B. Zhang, Realization of an Acoustic Third-Order Topological Insulator, Phys. Rev. Lett. **122**, 244301 (2019).

[5] M. Rodriguez-Vega, A. Kumar, and B. Seradjeh, Higher-order Floquet topological phases with corner and bulk bound states, Phys. Rev. B **100**, 085138 (2019).

[6] W. A. Benalcazar, B. A. Bernevig, and T. L. Hughes, Quantized electric multipole insulators, Science **357**, 61 (2017).

[7] Z. Song, Z. Fang, and C. Fang, (d- 2)-Dimensional Edge States of Rotation Symmetry Protected Topological States, Phys. Rev. Lett. **119**, 246402 (2017).

[8] M. Ezawa, Higher-Order Topological Insulators and Semimetals on the Breathing Kagome and Pyrochlore Lattices, Phys. Rev. Lett. **120**, 026801 (2018).

[9] L. Zou, H. C. Po, A. Vishwanath, and T. Senthil, Band structure of twisted bilayer graphene: Emergent symmetries, commensu-

rate approximants, and Wannier obstructions, Phys. Rev. B **98**, 085435 (2018).

[10] J. Ahn, S. Park, and B.-J. Yang, Failure of Nielsen-Ninomiya Theorem and Fragile Topology in Two-Dimensional Systems with Space-Time Inversion Symmetry: Application to Twisted Bilayer Graphene at Magic Angle, Phys. Rev. X **9**, 021013 (2019).

[11] Z.-D. Song, B. Lian, N. Regnault, and B. A. Bernevig, Twisted bilayer graphene. II. Stable symmetry anomaly, Phys. Rev. B **103**, 205412 (2021).

[12] B. Lian, F. Xie, and B. A. Bernevig, Landau level of fragile topology, Phys. Rev. B **102**, 041402(R) (2020).

[13] Q. S. Wu, J. Liu, Y. Guan, and O. V. Yazyev, Landau Levels Serve as Probe for Band Topology in Graphene Moiréé Superlattices, Phys. Rev. Lett. **126**, 056401 (2021).

[14] Y.-Z. Chou, F. Wu, and S. Das Sarma, Hofstadter butterfly and Floquet topological insulators in minimally twisted bilayer graphene, Phys. Rev. Res. **2**, 033271 (2020).

[15] Q. X. Lu, B. Lian, G. Chaudhary, B. A. Piot, G. Romagnoli, K. Watanabe, T. Taniguchi, M. Poggio, A. H. MacDonald, B. A. Bernevig *et al.*, Multiple flat bands and topological hofstadter butterfly in twisted bilayer graphene close to the second magic angle, Proc. Natl. Acad. Sci. **118**, e2100006118 (2021).

[16] B. Bradlyn, L. Elcoro, J. Cano, M. Vergniory, Z. Wang, C. Felser, M. I. Aroyo, and B. A. Bernevig, Topological quantum chemistry, Nature (London) **547**, 298 (2017).

[17] B. Bradlyn, Z. Wang, J. Cano, and B. A. Bernevig, Disconnected elementary band representations, fragile topology, and Wilson loops as topological indices: An example on the triangular lattice, Phys. Rev. B **99**, 045140 (2019).

[18] J. Cano, B. Bradlyn, Z. Wang, L. Elcoro, M. G. Vergniory, C. Felser, M. I. Aroyo, and B. A. Bernevig, Topology of Disconnected Elementary Band Representations, Phys. Rev. Lett. **120**, 266401 (2018).

[19] J. Cano, B. Bradlyn, Z. Wang, L. Elcoro, M. G. Vergniory, C. Felser, M. I. Aroyo, and B. A. Bernevig, Building blocks of topological quantum chemistry: Elementary band representations, Phys. Rev. B **97**, 035139 (2018).

[20] H. C. Po, H. Watanabe, and A. Vishwanath, Fragile Topology and Wannier Obstructions, Phys. Rev. Lett. **121**, 126402 (2018).

[21] A. Bouhon, A. M. Black-Schaffer, and R.-J. Slager, Wilson loop approach to fragile topology of split elementary band representations and topological crystalline insulators with time-reversal symmetry, Phys. Rev. B **100**, 195135 (2019).

[22] A. Bouhon, T. Bzdušek, and R.-J. Slager, Geometric approach to fragile topology beyond symmetry indicators, Phys. Rev. B **102**, 115135 (2020).

[23] V. Peri, Z.-D. Song, B. A. Bernevig, and S. D. Huber, Fragile Topology and Flat-Band Superconductivity in the Strong-Coupling Regime, Phys. Rev. Lett. **126**, 027002 (2021).

[24] Z.-D. Song, L. Elcoro, and B. A. Bernevig, Twisted bulk-boundary correspondence of fragile topology, Science **367**, 794 (2020).

[25] M. B. de Paz, M. G. Vergniory, D. Bercioux, A. García-Etxarri, and B. Bradlyn, Engineering fragile topology in photonic crystals: Topological quantum chemistry of light, Phys. Rev. Res. **1**, 032005(R) (2019).

[26] R.-X. Zhang and Z.-C. Yang, Tunable fragile topology in Floquet systems, Phys. Rev. B **103**, L121115 (2021).

[27] V. Peri, Z.-D. Song, M. Serra-Garcia, P. Engeler, R. Queiroz, X. Huang, W. Deng, Z. Liu, B. A. Bernevig, and S. D. Huber, Experimental characterization of fragile topology in an acoustic metamaterial, Science **367**, 797 (2020).

[28] J. Yu, Y. Ge, and S. Das Sarma, Dynamical fragile topology in Floquet crystals, Phys. Rev. B **104**, L180303 (2021).

[29] J. Kruthoff, J. de Boer, J. van Wezel, C. L. Kane, and R.-J. Slager, Topological Classification of Crystalline Insulators Through Band Structure Combinatorics, Phys. Rev. X **7**, 041069 (2017).

[30] R.-J. Slager, A. Mesaros, V. Juri, and J. Zaanen, The space group classification of topological band-insulators, Nat. Phys. **9**, 98 (2013).

[31] C. S. Chiu, D.-S. Ma, Z.-D. Song, B. A. Bernevig, and A. A. Houck, Fragile topology in line-graph lattices with two, three, or four gapped flat bands, Phys. Rev. Res. **2**, 043414 (2020).

[32] D.-S. Ma, Y. Xu, C. S. Chiu, N. Regnault, A. A. Houck, Z. Song, and B. A. Bernevig, Spin-Orbit-Induced Topological Flat Bands in Line and Split Graphs of Bipartite Lattices, Phys. Rev. Lett. **125**, 266403 (2020).

[33] A. Luo, Z. Song, and G. Xu, Fragile topological band in the checkerboard antiferromagnetic monolayer FeSe, npj Comput. Mater. **8**, 26 (2022).

[34] C. Shang, X. Zang, W. Gao, U. Schwingenschlögl, and A. Manchon, Second-order topological insulator and fragile topology in topological circuitry simulation, arXiv:2009.09167.

[35] Z. Wang, B. J. Wieder, J. Li, B. Yan, and B. A. Bernevig, Higher-Order Topology, Monopole Nodal Lines, and the Origin of Large Fermi Arcs in Transition Metal Dichalcogenides, Phys. Rev. Lett. **123**, 186401 (2019).

[36] G. F. Lange, A. Bouhon, and R.-J. Slager, Subdimensional topologies, indicators, and higher order boundary effects, Phys. Rev. B **103**, 195145 (2021).

[37] J. Herzog-Arbeitman, Z.-D. Song, N. Regnault, and B. A. Bernevig, Hofstadter Topology: Noncrystalline Topological Materials at High Flux, Phys. Rev. Lett. **125**, 236804 (2020).

[38] D. R. Hofstadter, Energy levels and wave functions of Bloch electrons in rational and irrational magnetic fields, Phys. Rev. B **14**, 2239 (1976).

[39] J.-W. Rhim, K. Kim, and B.-J. Yang, Quantum distance and anomalous Landau levels of flat bands, Nature (London) **584**, 59 (2020).

[40] Y. Hwang, J.-W. Rhim, and B.-J. Yang, Geometric characterization of anomalous Landau levels of isolated flat bands, Nat. Commun. **12**, 6433 (2021).

[41] Y. Guan, A. Bouhon, and O. V. Yazyev, Landau levels of the euler class topology, Phys. Rev. Res. **4**, 023188 (2022).

[42] L. Wang and D.-X. Yao, Coexistence of spin-1 fermion and dirac fermion on the triangular kagome lattice, Phys. Rev. B **98**, 161403(R) (2018).

[43] D.-X. Yao, Y. L. Loh, E. W. Carlson, and M. Ma, XXZ and Ising spins on the triangular kagome lattice, Phys. Rev. B **78**, 024428 (2008).

[44] Y.-H. Chen, H.-S. Tao, D.-X. Yao, and W.-M. Liu, Kondo Metal and Ferrimagnetic Insulator on the Triangular Kagome Lattice, Phys. Rev. Lett. **108**, 246402 (2012).

[45] Y. L. Loh, D.-X. Yao, and E. W. Carlson, Dimers on the triangular kagome lattice, Phys. Rev. B **78**, 224410 (2008).

[46] Y. L. Loh, D.-X. Yao, and E. W. Carlson, Thermodynamics of Ising spins on the triangular kagome lattice: Exact analytical method and Monte Carlo simulations, Phys. Rev. B **77**, 134402 (2008).

[47] S. Kim, W. H. Han, I.-H. Lee, and K. Chang, Boron triangular kagome lattice with half-metallic ferromagnetism, Sci. Rep. **7**, 7279 (2017).

[48] M. Gonzalez, F. Cervantes-lee, and L. W. ter Haar, Structural and magnetic properties of the topologically n 2-D material $Cu_9F_2(cpa)_6$: A triangulated kagome-like hexagonal network of CU(ii) trimers interconnected by CU(ii) monomers, Mol. Cryst. Liq. Cryst. Sci. Technol., Sect. A **233**, 317 (1993).

[49] S. Maruti and L. W. ter Haar, Magnetic Properties of the "Two-dimensional Triangles-in-Triangles" Kagomé Lattice $Cu_9X_2(cpa)_6$ ($X=$F,Cl,Br), J. Appl. Phys. **75**, 5949 (1994).

[50] M. Mekata, M. Abdulla, T. Asano, H. Kikuchi, T. Goto, T. Morishita, and H. Hori, Magnetic ordering in triangulated kagomélattice compound, $Cu_9Cl_2(cpa)_6nH_2O$, J. Magn. Magn. Mater. **177-181**, 731 (1998).

[51] M. I. Aroyo, J. M. Perez-Mato, D. Orobengoa, E. Tasci, G. de la Flor, and A. Kirov, Crystallography online: Bilbao crystallographic server, Bulg. Chem. Commun. **43**, 183 (2011).

[52] M. I. Aroyo, J. M. Perez-Mato, C. Capillas, E. Kroumova, S. Ivantchev, G. Madariaga, A. Kirov, and H. Wondratschek, Bilbao crystallographic server: I. Databases and crystallographic computing programs, Z. Kristallogr. - Cryst. Mater. **221**, 15 (2006).

[53] M. I. Aroyo, A. Kirov, C. Capillas, J. Perez-Mato, and H. Wondratschek, Bilbao crystallographic server. ii. representations of crystallographic point groups and space groups, Acta Crystallogr., Sect. A: Found. Crystallogr. **62**, 115 (2006).

[54] J. Herzog-Arbeitman, A. Chew, D. K. Efetov, and B. A. Bernevig, Reentrant Correlated Insulators in Twisted Bilayer Graphene at 25T (2pi flux), Phys. Rev. Lett. **129**, 076401 (2022).

[55] I. Das, C. Shen, A. Jaoui, J. Herzog-Arbeitman, A. Chew, C.-W. Cho, K. Watanabe, T. Taniguchi, B. A. Piot, B. A. Bernevig *et al.*, Observation of re-entrant correlated insulators and interaction driven fermi surface reconstructions at one magnetic flux quantum per moire unit cell in magic-angle twisted bilayer graphene, arXiv:2111.11341.

[56] F. Yu, T. Wu, Z. Wang, B. Lei, W. Zhuo, J. Ying, and X. Chen, Concurrence of anomalous Hall effect and charge density wave in a superconducting topological kagome metal, Phys. Rev. B **104**, L041103 (2021).

[57] Z. Zhang, Z. Chen, Y. Zhou, Y. Yuan, S. Wang, J. Wang, H. Yang, C. An, L. Zhang, X. Zhu *et al.*, Pressure-induced reemergence of superconductivity in the topological kagome metal $C_sV_3Sb_5$, Phys. Rev. B **103**, 224513 (2021).

[58] B. R. Ortiz, S. M. L. Teicher, Y. Hu, J. L. Zuo, P. M. Sarte, E. C. Schueller, A. M. Milinda Abeykoon, M. J. Krogstad, S. Rosenkranz, R. Osborn, R. Seshadri, L. Balents, J. He, and S. D. Wilson, $C_sV_3Sb_5$: A Z_2 topological kagome metal with a superconducting ground state, Phys. Rev. Lett. **125**, 247002 (2020).